

When galaxies burst: enhanced shot-noise for line-intensity mapping in the JWST era

Ely D. Kovetz,^{1,*} Hovav Lazare,¹ Sarah Libanore,¹ Julian B. Muñoz,^{2,3} and Eleonora Vanzan^{4,1}

¹*Department of Physics, Ben-Gurion University of the Negev, Be'er Sheva 84105, Israel*

²*Department of Astronomy, The University of Texas at Austin, Austin, TX 78712, USA*

³*Cosmic Frontier Center, The University of Texas at Austin, Austin, TX 78712, USA*

⁴*School of Physics and Astronomy, Tel-Aviv University, Tel-Aviv 69978, Israel*

Recent JWST observations indicate that star formation at $z \sim 4 - 6$ is more stochastic than previously assumed, with rms log-SFR scatter ~ 0.6 dex at $M_h \sim 10^{11} M_\odot$, growing toward smaller halos and time-correlated on ~ 25 Myr. This is significantly higher than the typical ~ 0.3 dex phenomenological lognormal scatter assumed in standard line-intensity mapping (LIM) forecasts. We propagate the JWST-era burstiness through to the LIM shot-noise power spectrum and show that the result is a simple multiplicative correction: the deterministic shot noise multiplied by a line-dependent boost factor \mathcal{B}_λ derived in closed form by convolving the SFR correlation function with the stellar-population-synthesis kernel of each line. At $z \sim 6$, we find $\mathcal{B}_{\text{H}\alpha} \simeq 7$ and $\mathcal{B} \sim 2.5 - 3.5$ for longer-window tracers ([C II], CO, UV) — factors of $\sim 2 - 5$ above the standard prescription, and growing further toward higher redshift. The enhancement transforms the LIM landscape: it improves auto-spectrum detectability and suppresses lower-redshift interloper contamination, but degrades cosmological applications such as BAO that rely on a clean clustering measurement. Crucially, it also opens a new use of LIM as a diagnostic of high-redshift star-formation physics beyond the regime of individually resolved galaxies: *redshift tomography* of a single line constrains the amplitude and mass dependence of the burstiness, while *cross-line shot-noise correlations* probe its time coherence.

Introduction. JWST is rapidly transforming our picture of galaxy formation in the first billion years. The high-redshift universe it has revealed is more complicated than expected: the UV luminosity function at $z \gtrsim 10$ is brighter than pre-launch models predicted [1–5], the H α /UV ratio shows a wide spread at $z \sim 4 - 6$ [6, 7], and individual galaxies appear to undergo dramatic short-timescale fluctuations in their star-formation rates [8–12]. A common thread is the notion of *burstiness*: that star formation in early galaxies, especially in low-mass halos where stellar feedback is most disruptive, proceeds in episodic bursts rather than smoothly. This has long been a generic prediction of feedback-regulated star formation, and recent work has begun to turn it from a qualitative idea into a quantitative, empirically anchored description [7, 13–20].

Bursty star formation has profound implications for line-intensity mapping (LIM), the technique of measuring the aggregate redshifted line emission from all sources in cosmic volumes [21, 22]. The observable LIM power spectrum decomposes into clustering and shot-noise terms,

$$P_\lambda(k) = \bar{I}_\lambda^2 b_{\text{eff}}^2(\lambda) P_m(k) + P_{\text{shot}}^\lambda, \quad (1)$$

where \bar{I}_λ is the mean intensity in band λ , $b_{\text{eff}}(\lambda)$ the luminosity-weighted halo bias, $P_m(k)$ the linear matter power spectrum, and P_{shot}^λ integrates the second moment of $L_\lambda(M_h)$, the luminosity–halo-mass relation [23],

$$P_{\text{shot}}^\lambda = \mathcal{X}_\lambda^2 \int dM_h \frac{dn}{dM_h} \langle L_\lambda^2 \rangle(M_h) = P_{\text{shot}}^\lambda|_{\text{det.}} + P_{\text{shot}}^\lambda|_{\text{stoch.}}, \quad (2)$$

where dn/dM_h is the halo mass function (HMF) and $\mathcal{X}_\lambda \equiv cy_\nu/(4\pi)$ is the standard luminosity (L_λ) to intensity (I_λ) conversion factor (c is the speed of light and

$y_\nu \equiv d\chi/d\nu_{\text{obs}}$ the comoving distance per unit observed frequency). The decomposition $\langle L_\lambda^2 \rangle = \bar{L}_\lambda^2 + \text{Var}(L_\lambda)$ at fixed M_h separates two physically distinct contributions: the halo-discreteness term [23]

$$P_{\text{shot}}^\lambda|_{\text{det.}} = \mathcal{X}_\lambda^2 \int dM_h \frac{dn}{dM_h} \bar{L}_\lambda^2(M_h), \quad (3)$$

which arises purely from halo counting Poisson statistics under a deterministic luminosity–halo-mass relation, and the galaxy-stochasticity term $P_{\text{shot}}^\lambda|_{\text{stoch.}} = \mathcal{X}_\lambda^2 \int dM_h \frac{dn}{dM_h} \text{Var}(L_\lambda)(M_h)$, which captures fluctuations in the per-halo luminosity at fixed M_h . Standard LIM forecasts retain only the halo-discreteness term [24–28], occasionally augmenting it with a phenomenological lognormal scatter $\sigma_L \sim 0.3 - 0.5$ dex at fixed M_h calibrated to simulations [29, 30]; this σ_L captures the combined effect of multiple sources of scatter (feedback variability, halo assembly history, AGN [31]), but without direct calibration against burstiness-sensitive observables at high redshift.

The recent analysis by Muñoz et al. [7] (M26) changes this. By combining the UV luminosity function, galaxy clustering, and H α /UV ratio data, M26 infer a burstiness amplitude (the square root of the integrated star formation rate power spectrum, hence “PS”) $\sigma_{\text{PS}} \simeq 2.0 \pm 0.3$ at a pivot mass $M_h = 10^{11} M_\odot$ ¹ with mass dependence $d\sigma_{\text{PS}}/d\log_{10} M_h \simeq -0.5$, and a burst coherence time $\tau_{\text{PS}} \simeq 25_{-10}^{+30}$ Myr. This corresponds to a large rms log-SFR scatter $\sigma_x = \sigma_{\text{PS}}/\sqrt{2} \approx 0.6$ dex at the pivot mass, which grows toward smaller halos, precisely the regime LIM is designed to probe. While these inferences are model-dependent and should be tested against independent data, the central values are large enough to warrant a careful revisit of LIM forecasts to account for burstiness.

¹ M26 quote σ_{PS} at pivot $10^{10} M_\odot$, where $\sigma_{\text{PS}} \simeq 2.5 \pm 0.5$ depending on dataset (this also allows to fit high- z UVLFs [7–9]); propagating via their mass-dependence slope to $10^{11} M_\odot$ gives $\sigma_{\text{PS}} \simeq 2.0 \pm 0.3$.

* kovetz@bgu.ac.il

In this work we propagate the M26 framework through to LIM observables. The underlying idea is simple: if galaxies are bursty, their luminosities at fixed halo mass are scattered around the mean, and P_{shot}^λ no longer reduces to a \bar{L}_λ^2 integral. The size of the correction is set by the convolution of the SFR correlation function with the time response of each line. We carry out this calculation analytically in the M26 effective burstiness model, arriving at closed-form semi-analytic expressions for the auto and cross LIM shot noise that factorize into the standard deterministic integral times a line- and mass-dependent boost, and map out how the boost depends on σ_{PS} and τ_{PS} . These expressions are ready-to-use inputs for existing LIM forecasting pipelines [32–35], subject to the line-modeling assumptions discussed below. As we will demonstrate, the burstiness-induced enhancement of the shot noise improves detection prospects for the auto-power spectrum but degrades cosmological applications of high-redshift LIM that rely on a clean clustering measurement.

Per-halo boost. Adapting the M26 framework (see also [20, 39]), we model the SFR of a galaxy in a halo of mass M_h at cosmic time t as a mean-anchored lognormal,

$$\dot{M}_\star(M_h, t) = \bar{M}_\star(M_h, t) e^{x(M_h, t) - \sigma_x^2(M_h)/2}, \quad (4)$$

where x is a zero-mean Gaussian field with stationary Ornstein–Uhlenbeck (OU) autocorrelation [36] $\xi_x(\Delta t) = \sigma_x^2 e^{-|\Delta t|/\tau_{\text{PS}}}$ and $\sigma_x^2 = \sigma_{\text{PS}}^2/2$. To account for SFR history, the line luminosity is weighted by a stellar population synthesis (SPS) Green’s function [7, 37], $L_\lambda(M_h) = \int dt_a G_\lambda(t_a) \dot{M}_\star(M_h, t_{\text{obs}} - t_a)$. The shot noise, Eq.(2), depends on $\langle L_\lambda^2 \rangle = \bar{L}_\lambda^2 [1 + V_\lambda]$, defining $V_\lambda \equiv \text{Var}(L_\lambda)/\bar{L}_\lambda^2$ as the dimensionless luminosity variance at fixed M_h .

For a top-hat SPS window of effective width t_λ (a useful proxy for the time over which each line responds to recent star formation [7, 29]), the dimensionless luminosity variance reduces to a single integral (Appendix B):

$$V_\lambda(M_h) = \frac{2}{t_\lambda^2} \int_0^{t_\lambda} ds (t_\lambda - s) \left[e^{\sigma_x^2(M_h) e^{-s/\tau_{\text{PS}}}} - 1 \right]. \quad (5)$$

This expression is a closed-form, exact resummation of the lognormal-mapped Gaussian correlator $\xi_y(\Delta t) = \exp[\xi_x(\Delta t)] - 1$ convolved with the line window, valid for any σ_x^2 . Two limits are useful: for $\tau_{\text{PS}} \gg t_\lambda$ (long bursts, narrow window), $V_\lambda \rightarrow e^{\sigma_x^2} - 1$; for $\tau_{\text{PS}} \ll t_\lambda$ (broad window), $V_\lambda \simeq (2\tau_{\text{PS}}/t_\lambda) \int_0^1 du (e^{\sigma_x^2 u} - 1)/u$, parametrically much larger than the linearized $(\tau_{\text{PS}}/t_\lambda)\sigma_x^2$ scaling at large σ_x . Eq. (5) agrees with direct Monte Carlo realizations of the OU process at the percent level (Appendix B).

Boosted shot noise. We define the per-halo boost $B_\lambda(M_h) \equiv 1 + V_\lambda(M_h) = e^{\sigma_{\xi, \lambda}^2(M_h)}$ with $\sigma_{\xi, \lambda}^2 \equiv \ln[1 + V_\lambda]$ playing the role of an effective lognormal scatter for the line (to be compared with the phenomenological σ_L^2 of standard LIM forecasts). The total shot noise, Eq.(2), then becomes

$$P_{\text{shot}}^\lambda = \mathcal{X}_\lambda^2 \int dM_h \frac{dn}{dM_h} \bar{L}_\lambda^2(M_h) e^{\sigma_{\xi, \lambda}^2(M_h)}. \quad (6)$$

This is the central result of the paper. Compared with the deterministic (halo-discreteness) expression Eq. (3), the

only change is the per-halo enhancement factor $e^{\sigma_{\xi, \lambda}^2(M_h)}$ inside the integrand. Defining the mass-integrated boost,

$$\mathcal{B}_\lambda \equiv \frac{P_{\text{shot}}^\lambda}{P_{\text{shot}}^\lambda|_{\text{det.}}} = \frac{\int dM_h (dn/dM_h) \bar{L}_\lambda^2 e^{\sigma_{\xi, \lambda}^2(M_h)}}{\int dM_h (dn/dM_h) \bar{L}_\lambda^2}, \quad (7)$$

\mathcal{B}_λ is simply a \bar{L}_λ^2 -weighted average of the per-halo enhancement. Because σ_{PS} grows toward low M_h , the shot-noise boost is weighted toward low-mass halos. This makes LIM surveys uniquely sensitive to the burstiness of faint, individually unresolvable galaxies at high redshift.

Before we continue, it is worth emphasizing what this calculation does *not* change. The mean intensity $\bar{I}_\lambda = \mathcal{X}_\lambda \int (dn/dM_h) \bar{L}_\lambda$ and the luminosity-weighted bias $b_{\text{eff}}(\lambda) = [\int (dn/dM_h) b_h \bar{L}_\lambda] / [\int (dn/dM_h) \bar{L}_\lambda]$ in Eq. (1) are unchanged by burstiness in our convention. Note that the Green function $G_\lambda(t_a)$ does enter the clustering term as well, through $\bar{L}_\lambda(M_h) = \int dt_a G_\lambda(t_a) \langle \dot{M}_\star \rangle(M_h, t_{\text{obs}} - t_a)$; but because the mean-anchored convention Eq. (4) sets $\langle \dot{M}_\star \rangle$ exactly equal to its UVLF-calibrated value by construction, the OU process drops out of the first moment entirely.² Burstiness only survives in the second moment $\langle L_\lambda^2 \rangle$, where the OU correlator sets $V_\lambda(M_h)$. The asymmetry between clustering and shot noise is thus a feature of the mean-anchoring choice, not an inconsistency: in the M26 *median* convention \bar{I}_λ and b_{eff} would pick up factors of $e^{\sigma_x^2/2}$ that get absorbed into the star-formation efficiency (SFE) parameters, with identical observable predictions. The boost factor \mathcal{B}_λ itself, though, is convention-independent. The LIM shot-noise enhancement we describe is a physical effect, not a parametrization choice.

Line-modeling. Throughout the body of this paper we adopt the minimal ansatz $\bar{L}_\lambda(M_h) \propto \bar{M}_\star(M_h)$ with a line-independent proportionality (per-line κ_λ amplitudes only enter the prefactor of P_{shot}^λ and \bar{I}_λ , not \mathcal{B}_λ). This isolates the effect we wish to characterize, the propagation of SFR burstiness through the SPS Green’s function, with the line entering only through its effective window width t_λ . Real LIM line models involve metallicity-, ISM-, and feedback-dependent shape modifications of $\bar{L}_\lambda(M_h)$, and some are calibrated against data that already contain scatter, possibly leading to double-counting when our boost is applied verbatim. We discuss line-modeling considerations, and quantify the resulting shifts in \mathcal{B}_λ , in Appendix A.

Numerical estimates. We evaluate $V_\lambda(M_h)$ from Eq. (5) for four representative LIM tracers using top-hat proxies of effective width t_λ : H α ($t_\lambda = 7$ Myr, equivalent to BC03 [37] e-folding time $t_e = t_\lambda/2 \approx 3.5$ Myr; see Appendix B), UV continuum ($t_\lambda = 100$ Myr, $t_e \approx 50$ Myr), [C II] 158 μm ($t_\lambda = 50$ Myr [40]), and CO(1–0) ($t_\lambda = 80$ Myr [29, 42]). For H α and UV the top-hat agrees with the realistic exponential Green’s function to $\lesssim 7\%$ in $\sigma_{\xi, \lambda}^2$ across the relevant

² We adopt the time-stationary approximation $\langle \dot{M}_\star \rangle(t_{\text{obs}} - t_a) \approx \langle \dot{M}_\star \rangle(t_{\text{obs}})$ over the support of G_λ , valid to a few percent at $z \sim 6$ even for the longest UV window; under this approximation the Green function reduces to a line-dependent normalization in \bar{L}_λ . See Appendix B for the explicit calculation and further discussion.

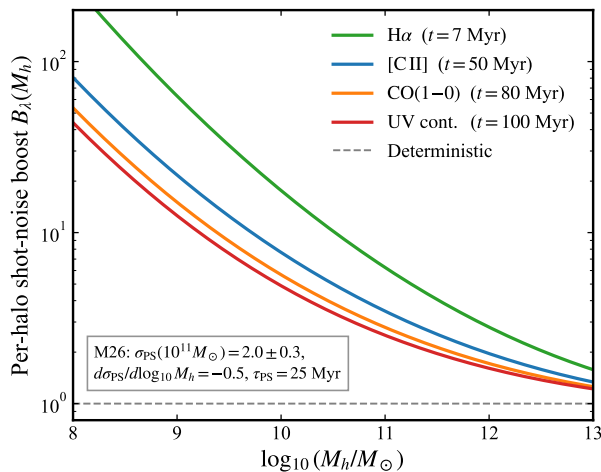


FIG. 1. **Per-halo shot-noise enhancement vs. halo mass for four representative LIM tracers at $z=6$, $\langle L_\lambda^2 \rangle / \bar{L}_\lambda^2 = e^{\sigma_{\xi,\lambda}^2(M_h)}$, relative to the deterministic prediction (dashed line at unity), for the M26 best-fit parameters [$\sigma_{\text{PS}}(10^{11} M_\odot) = 2.0 \pm 0.3$, $d\sigma_{\text{PS}}/d\log_{10} M_h = -0.5$, $\tau_{\text{PS}} = 25$ Myr]. Lines tracing recent star formation (H α) experience the largest per-halo enhancement, especially in low-mass halos where σ_{PS} peaks.**

mass range (see Appendix B for the matching prescription); for [C II] and CO, where the line response depends on ISM physics not captured by a single timescale, our quoted boosts are indicative only.

Fig. 1 shows the per-halo boost $e^{\sigma_{\xi,\lambda}^2(M_h)}$. The mass dependence is steep: H α shot noise per halo is enhanced by ~ 60 at $M_h = 10^9 M_\odot$, dropping to ~ 6 at $M_h = 10^{11} M_\odot$. Even the longer-timescale tracers experience per-halo enhancements of ~ 4 – 25 at the low-mass end (Tab. I).

Line (t_λ)	Per-halo boost $e^{\sigma_{\xi,\lambda}^2(M_h)}$			Mass-int. \mathcal{B}_λ
	$10^9 M_\odot$	$10^{10} M_\odot$	$10^{11} M_\odot$	
H α (7 Myr)	63	18	6.2	6.8
[C II] (50 Myr)	22	7.7	3.5	3.6
CO(1–0) (80 Myr)	15	5.7	2.8	2.9
UV cont. (100 Myr)	13	4.9	2.5	2.6

TABLE I. **Per-halo and mass-integrated shot-noise boosts at $z \approx 6$ for the M26 central burstiness parameters $\sigma_{\text{PS}}(10^{11} M_\odot) = 2.0$, $d\sigma_{\text{PS}}/d\log_{10} M_h = -0.5$, $\tau_{\text{PS}} = 25$ Myr, computed from Eq. (5). \mathcal{B}_λ uses the Sheth–Tormen [43] HMF via oLIMpus [35]/Zeus21 [34] (Planck 2018 cosmology, CLASS [44]) at $z = 6$, with an M26-style double power-law SFE for $\bar{L}_\lambda(M_h)$. The dominant systematic is the assumed σ_{PS} , displayed explicitly in Fig. 2.**

For the M26 central values, the mass-integrated boosts at $z \approx 6$ are $\mathcal{B}_{\text{H}\alpha} \simeq 6.8$, $\mathcal{B}_{[\text{C II}]} \simeq 3.6$, $\mathcal{B}_{\text{CO}} \simeq 2.9$, $\mathcal{B}_{\text{UV}} \simeq 2.6$. These are substantially larger than the $\sigma_L = 0.3$ dex phenomenological scatter routinely assumed in LIM forecasts [23, 29] (which yields a line-independent boost $e^{(\sigma_L \ln 10)^2} \simeq 1.6$), for two reasons: (i) σ_{PS} inferred by M26 is much larger than 0.3 dex, and (ii) the mass dependence weights the integral toward lower-mass halos where σ_{PS} is even larger. A third effect, the SPS Green’s function convolution that defines V_λ , pulls the boost down

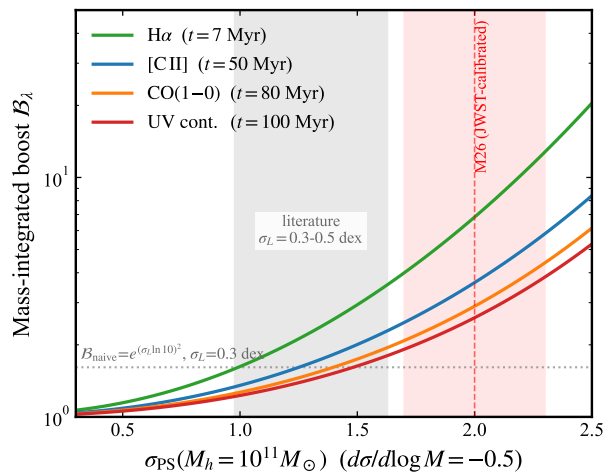


FIG. 2. **Sensitivity of the mass-integrated shot-noise boost \mathcal{B}_λ to the assumed burstiness amplitude σ_{PS} , at $z = 6$ with $\tau_{\text{PS}} = 25$ Myr and the M26 mass-dependent slope $d\sigma_{\text{PS}}/d\log_{10} M_h = -0.5$, plotted against the value at the pivot mass $M_h = 10^{11} M_\odot$. Red shaded band marks the M26 1σ region $\sigma_{\text{PS}} = 2.0 \pm 0.3$; gray band marks the literature $\sigma_L = 0.3$ – 0.5 dex region (translated to our σ_{PS} via $\sigma_{\text{PS}} = \sqrt{2} \ln(10) \sigma_L$). Dotted horizontal line marks the line- and mass-independent boost $e^{(\sigma_L \ln 10)^2} \simeq 1.6$ obtained under the literature $\sigma_L = 0.3$ dex prescription, lower by factors of ~ 2 – 5 than our \mathcal{B}_λ from M26 — a gap that translates directly into the gray dash-dot vs solid green offset in the absolute-units forecast of Fig. 3.**

for long-window lines relative to a naive $e^{\sigma_x^2}$ prescription using the M26 amplitude (Appendix B). Substituting phenomenological line-specific $\bar{L}_\lambda(M_h)$ shapes for H α , [O III], [C II], and CO into the boost integral shifts \mathcal{B}_λ at the -35% to $+17\%$ level relative to the $\bar{L}_\lambda \propto \bar{M}_*$ baseline (Appendix A).

Sensitivity to σ_{PS} . Because the boost depends exponentially on $\sigma_x^2 = \sigma_{\text{PS}}^2/2$, its absolute value is sensitive to the assumed burstiness amplitude. Fig. 2 shows \mathcal{B}_λ vs. σ_{PS} at the M26 mass-dependent slope, with the literature $\sigma_L = 0.3$ – 0.5 dex region marked for reference. For $\sigma_{\text{PS}} \lesssim 1$ the boost is modest, $\mathcal{B}_\lambda \lesssim 2$. At the M26 central value $\sigma_{\text{PS}} \simeq 2$, \mathcal{B}_λ ranges from ~ 2.6 for UV to ~ 6.8 for H α , factors of ~ 2 – 5 above the literature $\sigma_L = 0.3$ dex prescription. A measurement of P_{shot}^λ , given external estimates of $\bar{L}_\lambda(M_h)$, provides a direct route to σ_{PS} from LIM alone.

Observable impact. The full impact of the boost on observables is shown in Fig. 3: the H α LIM auto-power spectrum at $z=6$, with and without M26 burstiness, computed under the Yang+24 phenomenology with the M26 SFE substituted in for self-consistency. Burstiness leaves the clustering term unchanged in our convention; at large k the shot-noise tail is amplified by $\mathcal{B}_{\text{H}\alpha} \simeq 5.7$, lifting the bursty curve nearly an order of magnitude above its deterministic counterpart at $k \gtrsim 1 \text{ Mpc}^{-1}$, a striking change.

For survey-specific prospects (cf. Appendix A for line-modeling details), the M26 central values imply $\mathcal{B} \sim 4$ – 10 for H α at $z \sim 3$ – 8 , potentially detectable by SPHEREx [47] at the lower- z end of its sensitivity range, where H α sits well within its primary spectral coverage. For $\mathcal{B}_{[\text{C II}]} \sim 2$ – 6 at $z \sim 4$ – 8 , EXCLAIM [48] and CCAT/FYST [49] are well-positioned: forecasts for FYST [C II] find detectabil-

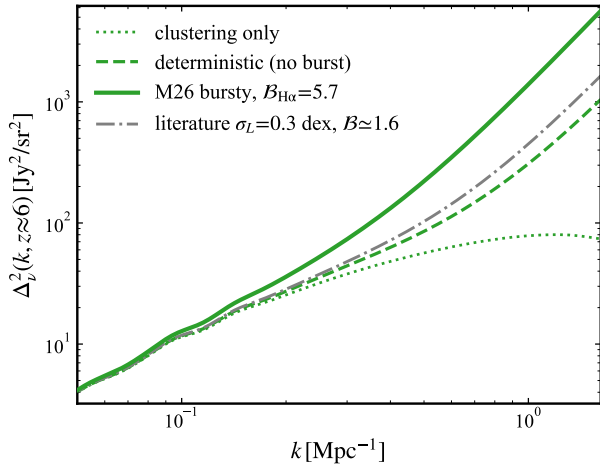


FIG. 3. $\text{H}\alpha$ LIM auto-power spectrum at $z \approx 6$, with and without M26 burstiness. Solid: full $\Delta_\nu^2(k)$ including the M26-boosted shot noise ($\mathcal{B}_{\text{H}\alpha} \simeq 5.7$). Dashed: deterministic prediction (no burstiness). Dotted: clustering component, unchanged between cases. Gray dash-dot: literature $\sigma_L = 0.3$ dex prescription, $\mathcal{B} \simeq 1.6$ — the standard pre-M26 LIM scatter ansatz, applied as a multiplicative correction to the same Yang+24 deterministic shot noise for visual reference; partition issues are discussed in Appendix A. $\text{H}\alpha$ uses the Yang+24 phenomenological $\bar{L}_{\text{H}\alpha}(M_h)$ shape with the M26 SFE substituted in for the underlying mean SFR; mean intensity, effective bias, and shot-noise normalization are taken directly from oLIMPus [35]. Both bursty and deterministic spectra are anchored to the same UVLF-calibrated mean SFR; they describe the same physical universe with $\langle \dot{M}_* \rangle$ matched to JWST data, differing only in whether the SFR scatter around that mean is at its M26 best-fit ($\sigma_{\text{PS}} = 2.0$, $\tau_{\text{PS}} = 25$ Myr) or zero. The boost factor here is slightly smaller than the $\bar{L} \propto \bar{M}_*$ baseline value of 6.8 in Tab. I, with the difference dictated by the Yang+24 shape; cf. Tab. II. See Fig. 7 (Appendix A) for the analogous figure at the survey-relevant redshifts of [C II] ($z = 6$, TIME/EXCLAIM/CCAT) and CO(1–0) ($z = 3$, COMAP).

ity of the [C II] power spectrum out to $z \approx 5.8$ (and potentially $z \approx 7.4$) depending on the adopted signal model [50], placing the $z = 6$ burst-enhanced signal (Appendix A) squarely in the detectable regime. For CO(1–0), $\mathcal{B}_{\text{CO}} \sim 2$ for COMAP-EoR [51] at $z \sim 5$ –8; at $z = 3$, the lower- z main sequence drives the kernel-peak halo mass to $\sim 10^{12} M_\odot$ where σ_{PS} is much smaller and the long Yang+21 SPS window further suppresses the boost to $\mathcal{B}_{\text{CO}} \simeq 1.6$. The implied bursty shot-noise power is well below the COMAP Season 2 upper limit [53] but may be accessible to the full 5-year campaign (pre-Season 2 forecast S/N 9–17 [52]).

It is important to caution that the redshift evolution above, and the redshift-tomography prediction below, assume the M26 amplitude and slope are themselves z -independent. This working assumption is not directly constrained by M26’s $z \sim 4$ –6 calibration; a measured deviation from these predictions would itself be diagnostic of z -evolution of the burstiness parameters. Quantifying detectability in specific configurations will require dedicated Fisher forecasts. Beyond this raw-amplitude effect, the spectral and tomographic structure of the boost provides two additional diagnostics of the underlying burstiness, which we now turn to.

Cross shot noise between lines. For two lines $\lambda_{1,2}$ at the same redshift, the cross-power spectrum is $P_{\lambda_1 \lambda_2}(k) = \bar{L}_1 \bar{L}_2 b_{\text{eff}}(\lambda_1) b_{\text{eff}}(\lambda_2) P_m(k) + P_{\text{shot}}^{\lambda_1 \lambda_2}$, with the same effective biases as in Eq. (1). Since different halos are uncorrelated, the cross shot noise is

$$P_{\text{shot}}^{\lambda_1 \lambda_2} = \mathcal{X}_1 \mathcal{X}_2 \int dM_h \frac{dn}{dM_h} \langle L_1 L_2 \rangle(M_h), \quad (8)$$

with the same-halo cross moment given by [7]

$$\langle L_1 L_2 \rangle - \bar{L}_1 \bar{L}_2 = \int \frac{d\omega}{2\pi} \tilde{W}_1^*(\omega) \tilde{W}_2(\omega) P_y(\omega). \quad (9)$$

This is the Fourier-space overlap of the two window functions weighted by the SFR power spectrum. Defining $\sigma_{\xi,12}^2(M_h) \equiv \ln[1 + \text{cov}(L_1, L_2) / (\bar{L}_1 \bar{L}_2)]$, we get

$$P_{\text{shot}}^{\lambda_1 \lambda_2} = \mathcal{X}_1 \mathcal{X}_2 \int dM_h \frac{dn}{dM_h} \bar{L}_1 \bar{L}_2 e^{\sigma_{\xi,12}^2(M_h)}. \quad (10)$$

Cross-correlation coefficient. To isolate the burst temporal structure from the deterministic luminosity relations, we construct a fractional-excess estimator. With $\Delta_{\lambda_1 \lambda_2} \equiv (P_{\text{shot}}^{\lambda_1 \lambda_2} / P_{\text{shot}}^{\lambda_1 \lambda_2}|_{\text{det}}) - 1$ (and analogously for the autospectra), we define

$$\mathcal{R}_{\lambda_1 \lambda_2} \equiv \frac{\Delta_{\lambda_1 \lambda_2}}{\sqrt{\Delta_{\lambda_1} \Delta_{\lambda_2}}}. \quad (11)$$

By construction, \mathcal{R} is the correlation coefficient of the *bursty excess* alone: the deterministic shot noise is divided out in numerator and denominator, leaving only the burstiness-induced contribution. The overall normalization of \bar{L}_λ cancels (only the shape of the L – M_h relation matters), and in the limit of mass-independent σ_{PS} the HMF cancels exactly, reducing \mathcal{R} to the per-halo Pearson correlation $V_{12} / \sqrt{V_1 V_2}$. In the M26 mass-dependent case it acquires a mild M_h -weighting. The asymptotic limits are $\mathcal{R} \rightarrow 1$ at $\tau_{\text{PS}} \rightarrow \infty$ (bursts coherent over arbitrarily long times, both windows seeing the same burst) and $\mathcal{R} \rightarrow \sqrt{\min(t_{\lambda_1}, t_{\lambda_2}) / \max(t_{\lambda_1}, t_{\lambda_2})}$ at $\tau_{\text{PS}} \rightarrow 0$ (geometric window overlap); the M26-favored regime $\tau_{\text{PS}} \sim 10$ –50 Myr lies in between, where the gradient with τ_{PS} is steepest. As a population-level analog of the resolved-galaxy $\text{H}\alpha$ /UV diagnostic of M26, \mathcal{R} probes τ_{PS} at redshifts where individual galaxies are too faint to be detected.

Fig. 4 shows $\mathcal{R}_{\lambda_1 \lambda_2}(\tau_{\text{PS}})$ for five line pairs, computed with the oLIMPus [35] HMF and M26 SFE. Pairs spanning very different timescales (e.g. $\text{H}\alpha \times \text{UV}$, $\text{H}\alpha \times \text{CO}$) carry the most τ_{PS} information, interpolating between the short- and long-burst limits across the M26-favored band; pairs with similar windows (CO \times UV) saturate near unity and serve as cross-checks. At the M26 best fit, $\mathcal{R}_{\text{H}\alpha \times \text{CO}} \approx 0.5$, between the long-burst ($\mathcal{R} \rightarrow 1$) and short-burst ($\mathcal{R} \rightarrow 0.3$) limits and providing a clean handle on τ_{PS} . The right panel maps $\mathcal{R}_{\text{H}\alpha, \text{CO}}$ over the M26 ($\sigma_{\text{PS}}, \tau_{\text{PS}}$) plane: isocontours are nearly vertical, confirming that \mathcal{R} depends primarily on τ_{PS} and only weakly on σ_{PS} . Within the M26 SFR-driven framework, $\mathcal{R} \geq 0$ follows from $\xi_x \geq 0$ and $W_\lambda \geq 0$; a measurement of $\mathcal{R} < 0$ would diagnose physics beyond M26 (e.g., SFR-correlated dust attenuation or feedback-mediated quenching).

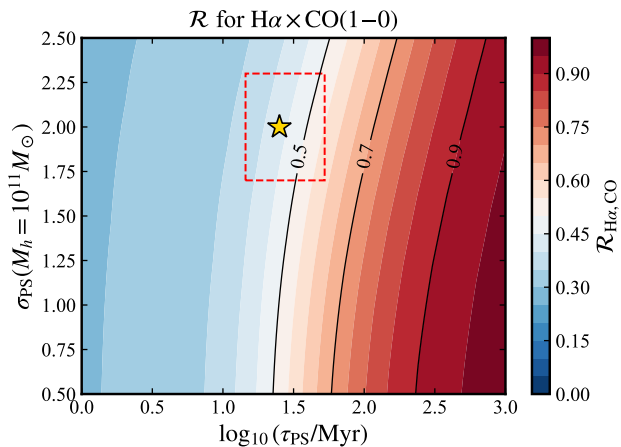
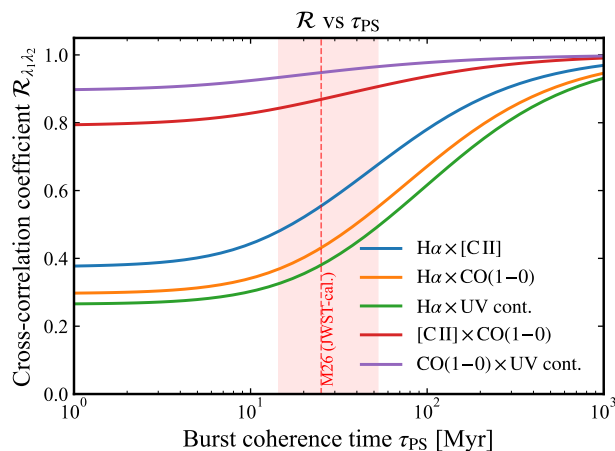


FIG. 4. **Line cross-correlation coefficient $\mathcal{R}_{\lambda_1\lambda_2}$ as a probe of the burst coherence time τ_{PS} .** \mathcal{R} is defined per Eq. (11) and isolates the bursty shot noise excess (by removing the deterministic luminosity weighting, leaving only the correlated stochastic excess). *Left:* \mathcal{R} vs. τ_{PS} for five line pairs. Pairs spanning very different temporal scales ($\text{H}\alpha \times \text{UV}$, $\text{H}\alpha \times \text{CO}$) carry the most τ_{PS} information; pairs with similar windows ($\text{CO} \times \text{UV}$) saturate near unity and serve as cross-checks. Vertical dashed line and red band mark the M26 1σ region for τ_{PS} . *Right:* $\mathcal{R}_{\text{H}\alpha, \text{CO}}$ over the M26 ($\sigma_{\text{PS}}(M_h^{\text{pivot}})$, τ_{PS}) plane. Near-vertical isocontours show \mathcal{R} depends primarily on τ_{PS} , only weakly on $\sigma_{\text{PS}}(M_h^{\text{pivot}})$. Yellow star: M26 central values; red dashed rectangle: M26 1σ region.

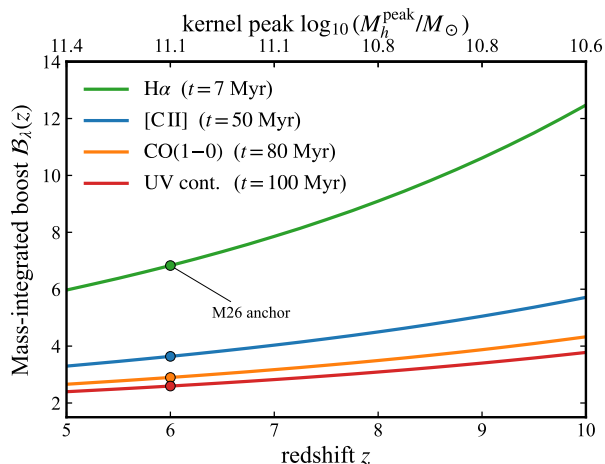


FIG. 5. **Redshift tomography of shot-noise boost.** $\mathcal{B}_\lambda(z)$ for our three representative lines $\text{H}\alpha$, $[\text{C II}]$, and $\text{CO}(1-0)$, computed using oLIMpus [35] and the M26 mass-dependent $\sigma_{\text{PS}}(M_h)$, with all other parameters held fixed. Markers indicate the M26 anchor at $z=6$. Top axis: the kernel-peak halo mass $\log_{10}(M_h^{\text{peak}}/M_\odot)$ at each redshift, computed from the $\bar{L}_\lambda^2(dn/d\ln M_h)$ weighting. As the HMF cutoff $M_*(z)$ falls with redshift, lower-mass halos with larger σ_{PS} dominate the integral, and \mathcal{B}_λ rises steeply. The $\text{H}\alpha$ boost grows from $\mathcal{B}_{\text{H}\alpha} \simeq 6.8$ at $z=6$ to $\mathcal{B}_{\text{H}\alpha} \simeq 12.5$ at $z=10$. Extrapolation to $z \sim 10$ is subject to caveats (see the text), including faint-end SFE evolution and breakdown of the lognormal description for $\sigma_{\text{PS}} \gtrsim 3$.

Redshift tomography. A complementary and arguably the most direct strategy for using LIM as a quantitative probe of mass-dependent burstiness is to observe the same emission line across multiple redshift bins. Because the $\bar{L}_\lambda^2(dn/d\ln M_h)$ kernel that drives shot noise tracks the HMF cutoff $M_*(z)$, the dominant halo mass shifts from $M_h \simeq 10^{11.1} M_\odot$ at $z=6$ to $\simeq 10^{10.6} M_\odot$ at $z=10$. Under the M26 slope $d\sigma_{\text{PS}}/d\log_{10} M_h = -0.5$, the kernel-peak σ_{PS} grows from $\simeq 2.0$ at $z=6$ to $\simeq 2.2$ at $z=10$, and $\mathcal{B}_\lambda(z)$ grows correspondingly: a factor of ~ 2 for $\text{H}\alpha$ be-

tween $z=6$ and $z=10$ (Fig. 5). Since the prediction depends only on the M26 slope and HMF evolution (per-line normalizations of \bar{L}_λ cancel in the boost ratio), it constitutes a direct test of M26’s mass-dependent burstiness picture. The main caveats to this are that the faint-end SFE evolution can shift $\mathcal{B}_\lambda(z)$ at the $\mathcal{O}(10\%)$ level, and that at $z \gtrsim 10$ the kernel of lines with extended low-mass $\bar{L}_\lambda(M_h)$ shapes can descend to halo masses where the implied $\sigma_{\text{PS}} \gtrsim 3$ approaches the regime in which gas depletion and stellar feedback regulate the SFR and the lognormal description of its scatter likely breaks down. The qualitative finding that \mathcal{B}_λ rises with z is robust to both effects.

Implications. What does an inflated shot noise mean for actual LIM experiments? In the shot-noise-dominated regime, P_{shot}^λ is itself a measurable signal, and one that, once the deterministic prediction is known, carries information about the underlying burstiness. Its amplitude, given external estimates of \bar{L}_λ and b_{eff} , constrains \mathcal{B}_λ and hence σ_{PS} , with degeneracies against the $\bar{L}_\lambda(M_h)$ relation, halo duty cycles, and selection effects partially broken by the same-redshift line ratio $P_{\text{shot}}^{\lambda_1}/P_{\text{shot}}^{\lambda_2}$. The cleanest probe of the *mass dependence* of σ_{PS} is the redshift tomography of Fig. 5: observing a single line across multiple z slides the LIM kernel in M_h in a calculable way and maps $\mathcal{B}_\lambda(z)$ onto $\sigma_{\text{PS}}(M_h)$ with the line itself as the calibrating common reference. Complementing this, the cross-line coefficient $\mathcal{R}_{\lambda_1\lambda_2}$ provides a handle on τ_{PS} specifically (Fig. 4), since it depends primarily on the relative SPS window widths. A further diagnostic is the LIM clustering-to-shot ratio, suggested as a means to reconstruct the LF [45]: this ratio is itself biased by \mathcal{B}_λ , so naive reconstruction yields a biased result, but with independent UVLF input the same ratio inverts into a measurement of \mathcal{B}_λ and hence σ_{PS} .

Mass-dependent burstiness brings a structural benefit for *interloper-line contamination*. Both the high- z target and any lower- z interloper line are boosted, but lower- z

interlopers originate from more massive halos with smaller σ_{PS} and are therefore less boosted than the target. The net effect is to raise the target-to-interloper signal ratio in the shot-noise tail, partially mitigating one of the main systematic concerns in high- z LIM. The size of this benefit depends on the redshift contrast and the mass scales involved and is best quantified survey-by-survey.

The shot-noise enhancement is, in the conventional reading, bad news for cosmology: in the clustering-dominated regime, an inflated stochastic floor lowers the effective number of accessible Fourier modes, shifting the scale at which boosted shot noise crosses the clustering term to larger physical scales and reducing the range of k over which features of $P_m(k)$ such as the baryon acoustic oscillations (BAOs) remain accessible above the floor; this can degrade BAO and expansion-rate measurements from future LIM surveys [58, 59]. The flip side is more attractive: the enhanced shot noise is itself a measurement, and an inversion of the problem recasts the LIM shot noise, through its z -tomography and cross-line ratio \mathcal{R} , as a probe of $\sigma_{\text{PS}}(M_h, z)$ and τ_{PS} at redshifts and halo masses inaccessible to resolved-galaxy spectroscopy.

Discussion. Several simplifications underlie our results. At fixed M_h we have taken L_λ lognormal, assumed uniform SPS Green’s functions across the galaxy population, and have not modeled bright-source masking or flux cuts. All these are straightforward refinements left to experimental forecasts. A few assumptions warrant further comment.

The OU correlator. The exponential form $\xi_x(\Delta t) = \sigma_x^2 e^{-|\Delta t|/\tau_{\text{PS}}}$ inherited from M26 has a non-differentiable cusp at $\Delta t = 0$, unphysical at the few-Myr timescale of cloud collapse and feedback. Substituting a smoother Gaussian kernel $\xi_x \propto e^{-\Delta t^2/(2\tau_{\text{PS}}^2)}$ at fixed τ_{PS} increases the per-halo V_λ by $\sim 20\%$ for H α and up to $\sim 90\%$ for UV, owing to the Gaussian’s larger integrated coherence ($\tau_{\text{PS}}\sqrt{\pi}/2$ vs. τ_{PS} for OU); matching the integrated coherence roughly halves these shifts. After mass integration the residual systematic on \mathcal{B}_λ is $\sim 10\%$ for H α and up to $\sim 50\%$ for the long-window tracers ([C II], CO, UV). Crucially, these shifts are *upward*: under any plausible alternative to OU, our boost numbers grow rather than shrink, so the conclusion that \mathcal{B}_λ exceeds the literature $\sigma_L = 0.3$ dex value of ~ 1.6 is robust against kernel choice.

Inter-halo SFR correlations. We have assumed halo-to-halo independence of $x(t)$. If burstiness is environmentally triggered (by mergers, filamentary accretion, large-scale assembly bias, reionization fronts, etc.), neighboring halos can have correlated fluctuations. This appears as a *scale-dependent* modification of b_{eff} at large scales, set by the correlation length of the trigger (negligible for merger-driven bursts of length corresponding to virial radii but potentially $\sim \text{Mpc}$ for accretion-driven bursts), together with a two-halo contribution to the shot-noise term. Both contributions are super-Poisson and would bias the inferred \mathcal{B}_λ *upward* from the per-halo value computed here. We defer quantitative estimates of these to future work.

Validity of the lognormal approximation. The shot-noise expression Eq. (6) depends only on the second moment of L_λ , which Eq. (5) computes *exactly* given the OU correlator; the lognormal interpretation merely labels the result

as $e^{\sigma_{\xi,\lambda}^2}$. M26 verify (their Appendix D) that the per-halo lognormal PDF for UV agrees with direct simulation at the $\sim 10\%$ level, sufficient for our applications. Statistics beyond the second moment, such as the voxel intensity distribution [54] or the line-intensity bispectrum [55], depend on higher cumulants of the SFR field and require the M26 short/long-timescale decomposition rather than the effective single-timescale framework adopted here.

Single-timescale assumption. Our OU autocorrelator $\xi_x(\Delta t) = \sigma_x^2 e^{-|\Delta t|/\tau_{\text{PS}}}$ assumes a single coherence time, while real galaxy star formation histories vary on a range of physical timescales: rapid fluctuations from individual star-forming regions, intermediate cycles driven by stellar feedback, and slower modulation from gas accretion and mergers [31]. For windows $t_\lambda \gg \tau_{\text{PS}}$ (UV, CO), the formalism correctly averages over many coherence times, but any long-timescale ($\gtrsim 100$ Myr) SFR variability beyond what M26’s H α /UV calibration constrains would add variance not captured here, modestly increasing \mathcal{B}_λ for the longer-window tracers. The H α window is short enough ($t_\lambda \sim \tau_{\text{PS}}/4$) that this concern does not apply.

Other sources of scatter. Our framework attributes all luminosity scatter at fixed halo mass to the M26 OU burstiness process. Additional non-burstiness scatter, from dust attenuation correlated with SFR, geometric/orientation effects, central-satellite distributions, or resonant radiative transfer for lines like Ly α [56, 57], would add in quadrature to σ_x^2 in our formalism; for non-burstiness scatter at the ~ 0.1 – 0.2 dex level the additional enhancement is at the ~ 20 – 30% level.

Conclusions. The picture of high-redshift star formation emerging from *JWST*, of large, time-correlated SFR scatter especially in the low-mass halos that dominate LIM signals, forces us to revisit predictions for the LIM shot noise. Adopting the M26 burstiness framework, we developed a formalism to consistently account for burstiness in LIM measurements and calculate how much the shot noise contribution is enhanced over the deterministic contribution from halo discreteness, as a function of halo mass.

For the M26 central values, the total, mass-integrated boosts at $z \sim 6$ are $\mathcal{B} \sim 2.5$ – 7 across our list of reference lines, growing to $\mathcal{B} \simeq 12.5$ for H α at $z \sim 10$ via redshift tomography. The boost depends exponentially on σ_{PS} and falls back to $\mathcal{B} \lesssim 2$ if $\sigma_{\text{PS}} \lesssim 1$ (Fig. 2). These are factors of 2 – 5 larger than the typically adopted values for scatter in LIM forecasts, with positive implications for detection.

The shot-noise enhancement also has consequences for cosmology: a higher stochastic floor obscures BAO features and degrades expansion-rate measurements [58, 59]. Conversely and more attractively, the LIM shot noise itself, in particular its z -tomography and cross-line ratio \mathcal{R} , can be inverted to constrain σ_{PS} and τ_{PS} at redshifts and halo masses inaccessible to resolved-galaxy spectroscopy.

Forthcoming work will integrate our results into Fisher forecasts for COMAP, EXCLAIM, SPHEREx, and FYST, and extend the formalism to higher-order statistics [60]. Another work will focus on the bursty 21cm signal, where the effect is both more subtle and more prominent [61].

ACKNOWLEDGMENTS

E.D.K. acknowledges support from the U.S.–Israel Binational Science Foundation (NSF-BSF grant 2022743 and BSF grant 2024193) and the Israel National Science Foundation (ISF grant 3135/25), as well as from the joint Israel–China program (ISF–NSFC grant 3156/23). H. L. is supported by a Negev PhD fellowship from the Kreitman school at BGU. E. V. is supported by an Azrieli International postdoctoral fellowship at TAU. J.B.M. acknowledges support from NSF Grants AST-2307354 and AST-2408637, and the NASA grant JWST-GO-03224.

APPENDIX A: LINE-MODELING CONSIDERATIONS

The body of this paper assumes the minimal ansatz $\bar{L}_\lambda(M_h) \propto \bar{M}_*(M_h)$, so that the boost factor \mathcal{B}_λ depends only on the temporal kernel t_λ and the M26 burstiness parameters ($\sigma_{\text{PS}}, \tau_{\text{PS}}$). Real LIM line models are richer than this: they invoke metallicity-, ISM-, and feedback-dependent modifications of the $\bar{L}_\lambda(M_h)$ shape, and some are calibrated against data that already contain galaxy-to-galaxy scatter. In this appendix we briefly classify the different kinds of line models in current use, quantify the resulting shifts in \mathcal{B}_λ when their $\bar{L}_\lambda(M_h)$ shapes are substituted into our boost integral, and flag a partition issue that arises when our boost is combined with luminosity-function-anchored prescriptions. We do not attempt a complete forecast revision here; that requires line-by-line and survey-by-survey treatment beyond the current scope.

Three classes of line-luminosity prescriptions. LIM forecasts in the literature fall into three broad categories that interact differently with our boost:

(i) *Mean-SFR-anchored.* $L_\lambda(M_h) = \kappa_\lambda \bar{M}_*(M_h)$ with \bar{M}_* tied to a UVLF-calibrated SFE. This is the framework adopted in the body of this work and in modern semi-numerical LIM codes [34, 35]. The boost applies cleanly: SFR scatter at fixed M_h is exactly what M26 quantifies, and the SPS Green’s function carries it to L_λ .

(ii) *Empirical $L(M_h)$ relations.* Power-law or double-power-law fits to the population-level L_λ – M_h relation, from semi-analytic galaxy formation models [40] or directly from simulations [28, 45]. These prescribe a deterministic $L_\lambda(M_h)$ shape with no explicit scatter; the implicit assumption is that the calibration data are well-described by their mean. Applying our boost on top is in principle clean, with one caveat: when the calibration is performed on a population that includes bursty galaxies, the dispersion is partially absorbed into the slope of the fit. Whether this constitutes a double-count depends on whether the calibration sample is representative of the M26 high-burstiness regime and left to the user to resolve.

(iii) *Direct LF-based forecasts.* Codes that integrate over an observed line luminosity function (LF) to predict shot noise [27–29, 42, 46–49]. The observed LF contains the physical scatter automatically. Therefore, multiplying their predicted P_{shot}^λ by our \mathcal{B}_λ re-anchors to the M26 burstiness inference and is informative as a consistency

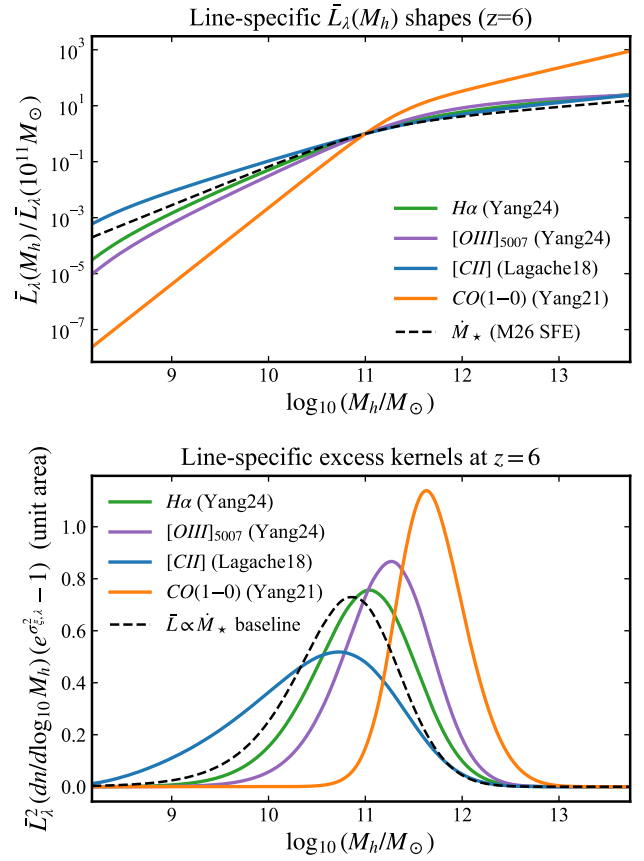


FIG. 6. **Line-specific shape modifications at $z = 6$.** *Top:* $\bar{L}_\lambda(M_h)$ for four phenomenological line models, each normalized to its value at $M_h = 10^{11} M_\odot$ and compared to the mean SFR shape (dashed black, M26 SFE). The [C II] Lagache+18 fit is sublinear at low mass; the Yang+21 CO(1–0) prescription is the most distinctive, with a steep low-mass cutoff and a super-linear high-mass slope, both reflecting metallicity- and shielding-dependent CO formation that is sharply truncated below a critical halo mass. *Bottom:* area-normalized excess kernels under each line-specific shape. Compared to the body’s $\bar{L}_\lambda \propto \bar{M}_*$ kernels, the peak of the CO excess shifts to higher M_h (driven by the steep low-mass CO cutoff), while the [C II] excess broadens to lower M_h (driven by the sublinear slope).

check, but a full predictive forecast would require modeling how the observed LF is itself generated by burstiness.

The phenomenological $L(M_h)$ models in class (ii) give the cleanest test of how line-specific $\bar{L}_\lambda(M_h)$ shapes shift our boost, and we use them below.

Line-specific shape modifications. We substitute the M26 SFE shape into oLIMpus and run four representative phenomenological line models: H α and [O III] $_{5007}$ (Yang+24), [C II] (Lagache+18 [40]), and CO(1–0) (Yang+21, extrapolated from the published $J = 2-1$ table). This isolates the effect of the line-specific $\bar{L}_\lambda(M_h)$ shape on the boost, with all other physics (HMF, $\sigma_{\text{PS}}(M_h)$, τ_{PS} , SPS window) held fixed to the body’s values. Fig. 6 shows the resulting $\bar{L}_\lambda(M_h)$ shapes (top, normalized at the M26 pivot $10^{11} M_\odot$) and the area-normalized excess kernels $\bar{L}_\lambda^2(dn/d\log_{10} M_h)(e^{\sigma_{\epsilon,\lambda}} - 1)$ at $z = 6$ (bottom).

The shifts in Table II are larger than the SPS-window

Line	t_λ [Myr]	\mathcal{B}_λ ($L \propto \bar{M}_*$)	\mathcal{B}_λ (line shape)	Δ [%]
H α	7	6.8	5.7	-17
[O III] ₅₀₀₇	7	6.8	4.8	-30
[C II]	50	3.6	4.3	+17
CO(1-0)	80	2.9	1.9	-35

TABLE II. Mass-integrated boosts at $z = 6$ under the body’s $\bar{L}_\lambda \propto \bar{M}_*$ ansatz versus four phenomenological $\bar{L}_\lambda(M_h)$ shapes (Yang+24 for H α and [O III], Lagache+18 for [C II], Yang+21 for CO), all evaluated at the M26 best-fit ($\sigma_{\text{PS}}, \tau_{\text{PS}}$). The line-specific shifts are dominated by where the $\bar{L}_\lambda^2(dn/d\log_{10} M_h)$ weighting kernel sits relative to the body’s pivot mass: shapes that up-weight low-mass halos (Lagache+18 [C II]) raise \mathcal{B}_λ via the larger $\sigma_{\text{PS}}(M_h < 10^{11} M_\odot)$ in the M26 slope, while shapes that up-weight high-mass halos (Yang+21 CO, Yang+24 short-lifetime lines) lower it. The full spread is roughly -35% to $+17\%$ relative to the baseline values copied from Tab. I.

approximation error ($\sim 7\%$, body Table I caption) but much smaller than the boost factors themselves. We therefore consider the body’s headline numbers ($\mathcal{B} \sim 7$ for short-window and $\mathcal{B} \sim 3$ for long-window tracers) robust at the factor-of-two level against the choice of line model.

Fig. 7 extends the body’s forecast to two more major LIM target lines at their experimentally relevant redshifts: [C II] at $z = 6$ (TIME [62], EXCLAIM [48], CCAT/FYST [49]) and CO(1-0) at $z = 3$ (COMAP Pathfinder [46], currently observing in the COMAP-allocated band $z = 2.4$ - 3.4). [C II] uses the Lagache+18 prescription with boost $\mathcal{B}_{[\text{C II}]} \simeq 4.3$; the high mean intensity ($\bar{I} \propto \rho_L/\nu_{\text{rest}}$ [63]) favors low-frequency lines) means shot noise dominates over clustering already at $k \gtrsim 0.2 \text{ Mpc}^{-1}$, with the bursty enhancement directly amplifying the dominant contribution to the auto-spectrum. CO(1-0) at $z = 3$ uses the Yang+21 metallicity-dependent prescription with boost $\mathcal{B}_{\text{CO}} \simeq 1.6$; the lower redshift puts the kernel-peak halo mass at $\sim 10^{12} M_\odot$, where $\sigma_{\text{PS}}(M_h)$ is much smaller per the M26 mass slope, and the long Yang+21 SPS window further suppresses the boost. The corresponding brightness temperature $\bar{T}_{\text{CO}} \simeq 0.7 \mu\text{K}$ places our prediction on the conservative end of the literature spread (e.g., the Li+16 [42] fiducial gives several times brighter), with the implied bursty shot-noise power $P_{\text{shot}} \simeq 3 \times 10^2 \mu\text{K}^2 \text{ Mpc}^3$ well below the COMAP Season 2 95% upper limit [53].

Scatter conventions and the SFE/burstiness partition. A subtler issue arises when our boost is applied on top of line models calibrated against the UVLF. Codes that derive their mean SFE by demanding the predicted UVLF match observations under an assumed scatter σ_L at fixed M_h (typically $\sigma_L = 0$ or ~ 0.3 dex) implicitly split the observed UVLF into two contributions: the assumed scatter and the inferred mean SFE together reproduce the data. The M26 inference, by contrast, simultaneously fits the UVLF, galaxy clustering, and the H α /UV ratio with a SFR scatter $\sigma_{\text{PS}} \simeq 2.0$. The two procedures correspond to physically different ways of allocating the same observed luminosity functions between mean-SFE and burstiness contributions: under the $\sigma_L \approx 0$ convention, the mean

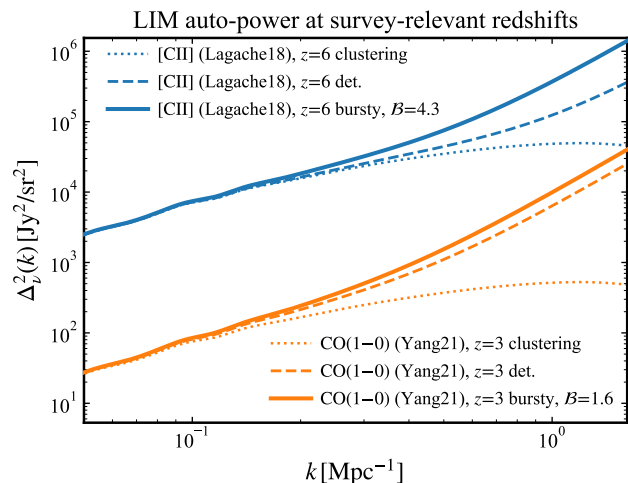


FIG. 7. **LIM auto-power spectra at survey-relevant redshifts.** Solid: full $\Delta_v^2(k)$ with M26 burstiness ($\sigma_{\text{PS}} = 2.0$, $\tau_{\text{PS}} = 25$ Myr); dashed: deterministic prediction (no burstiness); dotted: clustering component. [C II] at $z = 6$ uses the Lagache+18 prescription ($\bar{I}_{[\text{C II}]} \simeq 510 \text{ Jy/sr}$, $b_{\text{eff}} \simeq 2.6$, $\mathcal{B}_{[\text{C II}]} \simeq 4.3$); CO(1-0) at $z = 3$ uses the Yang+21 metallicity-dependent prescription ($\bar{I}_{\text{CO}} \simeq 17 \text{ Jy/sr}$, $b_{\text{eff}} \simeq 2.7$, $\mathcal{B}_{\text{CO}} \simeq 1.6$). Mean intensities and shot-noise normalizations are taken directly from oLIMpus [35] under each line model. For both lines, shot noise dominates over clustering across most of the LIM-accessible k range ($k \gtrsim 0.2 \text{ Mpc}^{-1}$ for [C II]; $k \gtrsim 0.1 \text{ Mpc}^{-1}$ for CO), so the burstiness enhancement directly amplifies the dominant contribution to the auto-spectrum. The visual impact differs sharply between the two lines: for [C II], the bursty curve sits a factor of ~ 4 above the deterministic prediction at high k , while for CO the $\mathcal{B}_{\text{CO}} \simeq 1.6$ is more modest.

SFE is large and there is no burst component, while in the M26 picture, the mean SFE is smaller and a substantial fraction of the observed UV emission comes from the bursty wing of the SFR distribution. Both conventions reproduce the UVLF; they differ in their predictions for the LIM clustering-to-shot ratio at fixed mean intensity.

For applying our boost cleanly, this means: forecasts that calibrate $L_\lambda(M_h)$ phenomenologically against observed *line* luminosity functions (most COMAP, SPHEREx, EXCLAIM, and CCAT-Prime forecasts) are not committed to a specific scatter convention, and multiplying their predicted P_{shot}^λ by our \mathcal{B}_λ provides an honest estimate of the bursty shot-noise enhancement under the M26 burstiness inference. Forecasts that compute L_λ via SFR-anchored conversions on top of a UVLF-calibrated SFE with $\sigma_L = 0$ implicitly assume a $\sigma_{\text{PS}} = 0$ universe. Applying our boost on top of such a prediction is internally inconsistent: it would correspond to a universe that simultaneously satisfies $\sigma_{\text{PS}} \simeq 2.0$ and the $\sigma_L = 0$ UVLF anchor, and would over-predict the LIM signal. A clean re-anchoring would require re-fitting the underlying SFE at the M26 mean, which is beyond the scope of this work. Future LIM measurements can resolve the partition empirically: the clustering-to-shot ratio, which is independent of the absolute amplitude calibration, is set by \mathcal{B}_λ for a given $\bar{L}_\lambda(M_h)$ shape and is the natural observable for distinguishing the two conventions [45].

We also note that we have not imposed an upper cap on $\sigma_{\text{PS}}(M_h)$ at low halo mass. Sufficiently large bursts ($\sigma_{\text{PS}} \gtrsim 3$) are physically self-limiting: such amplitudes would consume a low-mass halo's available cold gas on the burst-coherence timescale, requiring gas depletion and SN/radiative feedback to truncate the burst before this regime is reached. The lognormal description of the SFR PDF is also expected to break down here. At $z = 6$ the kernel-integrated boost is dominated by halos with $\sigma_{\text{PS}} \lesssim 2.5$, where neither concern applies. At higher redshift, lines with sublinear or extended low-mass $\bar{L}_\lambda(M_h)$ shapes (notably [C II] under Lagache+18) develop low-mass kernel tails reaching into the $\sigma_{\text{PS}} \gtrsim 3$ regime. Imposing a hard cap $\sigma_{\text{PS}} \leq 3$ shifts $\mathcal{B}_{[\text{C II}]}$ (Lagache+18) from -0.9% at $z=6$ to -5.1% at $z=10$, while H α , [O III], and CO are essentially unaffected (cap shifts $\lesssim 0.5\%$ across all redshifts). The redshift-tomography prediction in Fig. 5, which uses the body's $\bar{L} \propto \bar{M}_\star$ assumption, is robust against this systematic at the sub-percent level for H α across the full $z=5\text{--}15$ range.

APPENDIX B: DERIVATION OF $V_\lambda(M_h)$ AND VERIFICATION

Here we derive the closed-form expression for the per-halo luminosity variance Eq. (5) from the M26 SFR model, verify it against Monte Carlo realizations of the OU process, and show how the result compares with the trivial $e^{\sigma_x^2}$ stochasticity prescription used in most LIM literature.

Why the Green function survives only in the second moment. The mean line luminosity is $\bar{L}_\lambda(M_h, t_{\text{obs}}) = \int dt_a G_\lambda(t_a) \langle \dot{M}_\star \rangle(M_h, t_{\text{obs}} - t_a)$, where the lognormal expectation $\langle \dot{M}_\star \rangle = \bar{M}_\star \langle e^{x - \sigma_x^2/2} \rangle$ trivially equals the UVLF-anchored value, since $\langle e^x \rangle = e^{\sigma_x^2/2}$ exactly cancels the $e^{-\sigma_x^2/2}$ offset in the SFR definition Eq. (4). Throughout this work we adopt the time-stationary approximation $\langle \dot{M}_\star \rangle(M_h, t_{\text{obs}} - t_a) \approx \langle \dot{M}_\star \rangle(M_h, t_{\text{obs}})$ across the support of G_λ , justified at the few-percent level at $z \sim 6$ (cosmic time changes by $\sim 10\%$ over 100 Myr; SFRs in our halo-mass range change by less). Under this approximation the Green function in the first moment reduces to a line-dependent normalization, $\bar{L}_\lambda(M_h, t_{\text{obs}}) \approx \kappa_\lambda \langle \dot{M}_\star \rangle(M_h, t_{\text{obs}})$ with $\kappa_\lambda = \int dt_a G_\lambda(t_a)$. The second moment is fundamentally different because $\langle e^{x_1 + x_2} \rangle = e^{\sigma_x^2 + \xi_x(t_1 - t_2)}$ leaves the time correlator ξ_x uncanceled. The mean-anchoring choice thus routes burstiness exclusively into $\langle L_\lambda^2 \rangle$; relaxing the time-stationary approximation introduces a deterministic look-back correction to \bar{L}_λ that affects the clustering and shot-noise baselines together, leaving the boost $\mathcal{B}_\lambda \equiv P_{\text{shot}}/P_{\text{shot}|\text{det}}$ unchanged.

From SFR statistics to V_λ . The line luminosity is $L_\lambda(M_h) = \int_0^\infty dt_a G_\lambda(t_a) \dot{M}_\star(M_h, t_{\text{obs}} - t_a)$. Defining the window $W_\lambda(M_h, t_a) \equiv G_\lambda(t_a) \bar{M}_\star(M_h, t_{\text{obs}} - t_a)$ and writing $L_\lambda = \int W_\lambda y dt_a$ with $y \equiv e^{x - \sigma_x^2/2}$ (so $\langle y \rangle = 1$), the luminosity correlator is set by the lognormal-mapped Gaussian correlator [38, 39]

$$\xi_y(\Delta t) = \exp[\xi_x(\Delta t)] - 1, \quad (12)$$

which is *not* well approximated by ξ_x when $\sigma_x^2 \sim \mathcal{O}(1)$. The dimensionless luminosity variance at fixed M_h is then

$$V_\lambda(M_h) = \frac{\int dt_1 dt_2 W_\lambda(t_1) W_\lambda(t_2) \xi_y(t_1 - t_2)}{[\int dt_a W_\lambda]^2}. \quad (13)$$

V_λ depends on W_λ only through its autocorrelation:

$$V_\lambda = \int_0^\infty du \left[2 \int_0^\infty W_\lambda(t) W_\lambda(t+u) dt \right] [e^{\xi_x(u)} - 1]. \quad (14)$$

A top-hat of width t_λ has the same autocorrelation peak and integrated coherence as an exponential of e-folding $t_e = t_\lambda/2$, which is the matching prescription we adopt for our t_λ values. For H α and UV, where the Green's function is set by stellar physics, direct numerical comparison of the top-hat and exponential forms via Eq. (13) confirms agreement at the $\lesssim 5\%$ level in $\sigma_{\xi, \lambda}^2(M_h) = \ln[1 + V_\lambda(M_h)]$ across the relevant mass range.

For an OU correlator $\xi_x(\Delta t) = \sigma_x^2 e^{-|\Delta t|/\tau_{\text{PS}}}$, the spectral density of y admits a closed form. Expanding ξ_y as a Taylor series and Fourier-transforming term by term gives

$$P_y(\omega) = \sum_{n=1}^\infty \frac{(\sigma_x^2)^n}{n!} \frac{2n\tau_{\text{PS}}}{n^2 + (\omega\tau_{\text{PS}})^2}, \quad (15)$$

each term being a Lorentzian of width n/τ_{PS} . The series converges very rapidly because the n -th term scales as $(\sigma_x^2)^n/n!$, so P_y is an entire function of σ_x^2 with no convergence concern at any amplitude we encounter; the $n \geq 2$ terms are the non-Gaussian enhancement, and dominate V_λ when $\sigma_x^2 \sim \mathcal{O}(1)$. Substituting Eq. (15) into a top-hat window of width t_λ and performing the Fourier transform yields the body's Eq. (5), which is exact for any σ_x^2 .

For $\tau_{\text{PS}} \gg t_\lambda$ the integrand approaches $e^{\sigma_x^2} - 1$ uniformly, giving $V_\lambda \rightarrow e^{\sigma_x^2} - 1$. For $\tau_{\text{PS}} \ll t_\lambda$ the integral is dominated by $s \lesssim \tau_{\text{PS}}$, yielding $V_\lambda \simeq (2\tau_{\text{PS}}/t_\lambda) \int_0^1 du (e^{\sigma_x^2 u} - 1)/u$ via the substitution $u = e^{-s/\tau_{\text{PS}}}$ in the leading-order asymptotic expansion, which is parametrically much larger than the $(\tau_{\text{PS}}/t_\lambda)\sigma_x^2$ scaling that would obtain if one substituted ξ_x for ξ_y . As a quantitative check, for UV continuum at $M_h = 10^{11} M_\odot$ (where $\sigma_x^2 = 2.0$ at our central values), Eq. (5) gives $V_\lambda \simeq 1.5$ versus a linearized $V_\lambda \simeq 0.76$; at $M_h = 10^{10} M_\odot$ ($\sigma_x^2 \simeq 3.1$) the exact $V_\lambda \simeq 3.9$ exceeds the linearized estimate $V_\lambda \simeq 1.2$ by more than a factor of three. This non-Gaussian enhancement at large σ_x^2 is what drives the boost values reported in the body.

Monte Carlo verification. We verified Eq. (5) against Monte Carlo realizations of the OU process for representative cases ($t_\lambda = 7, 50, 100$ Myr at $\sigma_{\text{PS}} = 2.0$, $\tau_{\text{PS}} = 25$ Myr). Across 10 batches of 10^6 realizations each, the closed form lies within the sampling spread of the MC estimator at all three timescales (no systematic bias detected); the per-batch scatter of the MC estimator itself is large ($\sim 1\text{--}3\%$, growing with t_λ), reflecting the heavy-tailed sampling of the lognormal L_λ rather than any deficiency of Eq. (5).

Comparison with the trivial $e^{\sigma_x^2}$ prescription. Earlier LIM forecasts often introduce per-galaxy stochasticity by simply multiplying the deterministic shot noise by $e^{(\sigma_L \ln 10)^2}$ with a phenomenological $\sigma_L \sim 0.3$ dex calibrated against

simulations, without convolving against the SPS Green’s function. Our framework departs from this in three ways: (i) the M26-inferred σ_{PS} is much larger than 0.3 dex; (ii) the mass dependence weights the integral toward lower-mass halos where σ_{PS} is even larger; and (iii) the Green-function convolution that defines V_λ encodes the time response of each line. Effects (i) and (ii) push the boost *up* relative to the literature prescription; effect (iii) pushes it *down* relative to a naive $e^{\sigma_x^2} - 1$ result using the M26 amplitude, because time-averaging across a broad SPS win-

dow partially smooths the bursts. For long-window tracers (UV, CO, [C II]) the latter effect can be substantial, reducing the per-halo boost by factors of a few relative to the $\tau_{\text{PS}} \gg t_\lambda$ asymptote. The two corrections combine to give the modest factor $\mathcal{B}_\lambda \sim 1.5\text{--}3$ enhancement of long-window boosts relative to the $\sigma_L = 0.3$ dex literature reference (compared with $\sim 4\text{--}5$ for H α , where the Green-function effect is small); the dotted reference line in Fig. 2 marks the literature value.

-
- [1] C. A. Mason, M. Trenti, T. Treu, “The brightest galaxies at cosmic dawn”, *MNRAS* **521**, 497 (2023).
- [2] Y. Harikane *et al.*, “A Comprehensive Study of Galaxies at $z \sim 9\text{--}16$ Found in the Early JWST Data: Ultraviolet Luminosity Functions and Cosmic Star Formation History at the Pre-reionization Epoch”, *Astrophys. J.* **265**, 5 (2023).
- [3] S. L. Finkelstein *et al.*, “The Complete CEERS Early Universe Galaxy Sample”, *Astrophys. J. Lett.* **969**, L2 (2024).
- [4] C. T. Donnan *et al.*, “JWST PRIMER: a new multifield determination of the evolving galaxy UV luminosity function at redshifts $z \simeq 9\text{--}15$ ”, *MNRAS* **533**, 3222 (2024).
- [5] B. E. Robertson *et al.*, “Earliest Galaxies in the JADES Origins Field: Luminosity Function and Cosmic Star Formation Rate Density 300 Myr after the Big Bang”, *Astrophys. J.* **970**, 31 (2024).
- [6] R. Endsley *et al.*, “The star-forming and ionizing properties of dwarf $z \sim 6\text{--}9$ galaxies in JADES: insights on bursty star formation and ionized bubble growth”, *MNRAS* **533**, 1111 (2024).
- [7] J. B. Muñoz, J. Chisholm, G. Sun, J. Samuel, J. Mirocha, E. Bregou, A. Venditti, M. Qezlou, C. Simmonds and R. Endsley, “Relatively Fast and Reasonably Furious: Evidence for Increased Burstiness in Smaller Halos at Cosmic Dawn,” [arXiv:2601.07912].
- [8] G. Sun, C. A. Faucher-Giguère, C. C. Hayward, X. Shen, A. Wetzel and R. K. Cochrane, “Bursty Star Formation Naturally Explains the Abundance of Bright Galaxies at Cosmic Dawn,” *Astrophys. J. Lett.* **955**, no.2, L35 (2023)
- [9] V. Gelli, C. Mason, C. C. Hayward, “The impact of mass-dependent stochasticity at cosmic dawn”, *ApJ* **975**, 192 (2024).
- [10] A. Pallottini and A. Ferrara, “Stochastic star formation in early galaxies: JWST implications”, *Astron. Astrophys.* **677**, L4 (2023).
- [11] I. Mitsuhashi *et al.*, “UNCOVER/MegaScience Finds Uniform and Highly Bursty Star Formation at $3 < z < 9$, consistent with the High-Redshift UV Luminosity Function”, [arXiv:2601.16284].
- [12] L. Clarke, A. E. Shapley, R. L. Sanders, M. W. Topping, G. B. Brammer, T. Bento, N. A. Reddy *et al.*, “The Star-Forming Main Sequence in JADES and CEERS at $z > 1.4$: Investigating the Burstiness of Star Formation”, *Astrophys. J.* **977**, 133 (2024).
- [13] P. F. Hopkins, D. Kereš, J. Oñorbe, C.-A. Faucher-Giguère, E. Quataert, N. Murray, J. S. Bullock, “Galaxies on FIRE (Feedback In Realistic Environments)”, *MNRAS* **445**, 581 (2014).
- [14] M. Sparre, C. C. Hayward, R. Feldmann, C.-A. Faucher-Giguère, A. L. Muratov, D. Kereš, P. F. Hopkins, “Observational signatures of bursty star formation in galaxies”, *MNRAS* **466**, 88 (2017).
- [15] K. El-Badry, A. Wetzel, M. Geha, P. F. Hopkins, D. Kereš, T. K. Chan, C.-A. Faucher-Giguère, “Breathing FIRE: How Stellar Feedback Drives Radial Migration, Rapid Size Fluctuations, and Population Gradients in Low-Mass Galaxies”, *Astrophys. J.* **820**, 131 (2016).
- [16] C.-A. Faucher-Giguère, “A model for the origin of bursty star formation in galaxies”, *MNRAS* **473**, 3717 (2018).
- [17] S. Tacchella, J. C. Forbes, N. Caplar, “Stochastic modeling of star-formation histories II”, *MNRAS* **497**, 698 (2020).
- [18] S. R. Furlanetto and J. Mirocha, “Bursty star formation during the Cosmic Dawn driven by delayed stellar feedback”, *MNRAS* **511**, 3895 (2022).
- [19] J. B. Muñoz, J. Mirocha, S. Furlanetto, N. Sabti, “Breaking degeneracies in the first galaxies with clustering”, *MNRAS Letters* **526**, L47 (2023).
- [20] G. Sun, J. B. Muñoz, J. Mirocha, C.-A. Faucher-Giguère, “Constraining bursty star formation histories with galaxy UV and H α luminosity functions and clustering”, [arXiv:2410.21409].
- [21] J. L. Bernal and E. D. Kovetz, “Line-Intensity Mapping: Theory Review”, *Astron. Astrophys. Rev.* **30**, 5 (2022).
- [22] E. D. Kovetz *et al.*, “Line-Intensity Mapping: 2017 Status Report”, [arXiv:1709.09066].
- [23] E. Schaane and M. White, “Astrophysics & cosmology from LIM vs galaxy surveys”, *JCAP* **2021**, 067 (2021).
- [24] A. Lidz, S. R. Furlanetto, S. P. Oh, J. Aguirre, T.-C. Chang, O. Doré, J. R. Pritchard, “Intensity Mapping with Carbon Monoxide Emission Lines and the Redshifted 21 cm Line” *Astrophys. J.* **741**, 70 (2011).
- [25] A. R. Pullen, O. Doré, J. Bock, “Intensity Mapping across Cosmic Times with the Ly α Line”, *ApJ* **786**, 111 (2014).
- [26] P. C. Breyse, E. D. Kovetz and M. Kamionkowski, “The high redshift star-formation history from carbon-monoxide intensity maps,” *MNRAS* **457**, L127 (2016)
- [27] P. C. Breyse, E. D. Kovetz, M. Kamionkowski, “Carbon monoxide intensity mapping at moderate redshifts”, *MNRAS* **443**, 3506 (2014).
- [28] B. Yue, A. Ferrara, A. Pallottini, S. Gallerani, L. Vallini, “Intensity mapping of [C II] emission from early galaxies”, *MNRAS* **450**, 3829 (2015).
- [29] G. Sun *et al.*, “Probing Cosmic Reionization and Molecular Gas Growth with TIME”, *ApJ* **915**, 33 (2021).
- [30] S. Yang, A. R. Pullen, E. R. Switzer, “Evidence for [CII] diffuse line emission at redshift $z \sim 2.6$ ”, *MNRAS* **489**, L53 (2019).
- [31] K. G. Iyer, S. Tacchella, S. Genel *et al.*, “The diversity and variability of star formation histories in models of galaxy evolution”, *Mon. Not. Roy. Astron. Soc.* **498**, 430 (2020).
- [32] L. Mas-Ribas, G. Sun, T.-C. Chang, M. O. Gonzalez, R. H. Mebane, “LIMFAST. I. A Seminumerical Tool for Line

- Intensity Mapping”, *Astrophys. J.* **950**, 39 (2023).
- [33] G. Sun, L. Mas-Ribas, T.-C. Chang, S. R. Furlanetto, R. H. Mebane, M. O. Gonzalez, J. Parsons, A. C. Trapp, “LIMFAST. II. Line Intensity Mapping as a Probe of High-redshift Galaxy Formation”, *ApJ* **950**, 40 (2023).
- [34] J. B. Muñoz, “An Effective Model for the Cosmic-Dawn 21-cm Signal”, *MNRAS* **523**, 2587 (2023).
- [35] S. Libanore, J. B. Muñoz, E. D. Kovetz, “Effective model for LIM: Auto- and cross-power spectra in the cosmic dawn and reionization”, *PRD* **112**, 083552 (2025).
- [36] G. E. Uhlenbeck and L. S. Ornstein, “On the Theory of the Brownian Motion,” *Phys. Rev.* **36**, 823 (1930).
- [37] G. Bruzual and S. Charlot, “Stellar population synthesis at the resolution of 2003”, *MNRAS* **344**, 1000 (2003).
- [38] H. S. Xavier, F. B. Abdalla, B. Joachimi, “Improving log-normal models for cosmological fields”, *MNRAS* **459**, 3693 (2016).
- [39] N. Caplar and S. Tacchella, “Stochastic modeling of star-formation histories I: the scatter of the star-forming main sequence”, *MNRAS* **487**, 3845 (2019).
- [40] G. Lagache, M. Cousin, M. Chatzikos, “Full disc [C II] mapping of nearby star-forming galaxies”, *Astron. Astrophys.* **609**, A130 (2018).
- [41] R. C. Kennicutt, “Star Formation in Galaxies Along the Hubble Sequence”, *Annu. Rev. Astron. Astrophys.* **36**, 189 (1998).
- [42] T. Y. Li, R. H. Wechsler, K. Devaraj, S. E. Church, “Connecting CO Intensity Mapping to Molecular Gas and Star Formation in the Epoch of Galaxy Assembly”, *Astrophys. J.* **817**, 169 (2016).
- [43] R. K. Sheth and G. Tormen, “Large-scale bias and the peak background split”, *MNRAS* **308**, 119 (1999).
- [44] J. Lesgourgues, “The Cosmic Linear Anisotropy Solving System (CLASS) I: Overview”, *arXiv:1104.2932* (2011).
- [45] B. Yue and A. Ferrara, “Studying high- z galaxies with [CII] intensity mapping,” *MNRAS* **490**, 1928 (2019),
- [46] K. A. Cleary *et al.* “COMAP Early Science. I. Overview”, (COMAP Collab.), *Astrophys. J.* **933**, 182 (2022).
- [47] O. Doré *et al.*, “Cosmology with the SPHEREX All-Sky Spectral Survey”, [*arXiv:1412.4872*].
- [48] G. Cataldo *et al.*, “Overview and status of EXCLAIM, the experiment for cryogenic large-aperture intensity mapping”, *JATIS* **7**, 011007 (2021).
- [49] CCAT-Prime Collab., M. Aravena *et al.*, “CCAT-prime Collaboration: Science Goals and Forecasts with Prime-Cam on the Fred Young Submillimeter Telescope”, *Astrophys. J. Suppl.* **264**, 7 (2023).
- [50] C. Karoumpis, B. Magnelli, E. Romano-Díaz, M. Haslbauer, F. Bertoldi, “[CII] line intensity mapping the epoch of reionization with the Prime-Cam on FYST”, *Astron. Astrophys.* **659**, A12 (2022).
- [51] P. C. Breyse *et al.*, “COMAP Early Science: VII. Prospects for CO Intensity Mapping at Reionization”, *Astrophys. J.* **933**, 188 (2022).
- [52] D. T. Chung *et al.* (COMAP Collab.), “COMAP Early Science: V. Constraints and Forecasts at $z \sim 3$ ”, *Astrophys. J.* **933**, 186 (2022).
- [53] N.-O. Stutzer *et al.* (COMAP Collab.), “COMAP Pathfinder – Season 2 results II. Updated constraints on the CO(1–0) power spectrum”, *Astron. Astrophys.* **691**, A337 (2024) [*arXiv:2406.07511*].
- [54] P. C. Breyse, E. D. Kovetz, P. S. Behroozi, L. Dai, and M. Kamionkowski, “Insights from probability distribution functions of intensity maps,” *MNRAS* **467**, 2996 (2017),
- [55] A. Moradinezhad Dizgah and G. K. Keating, “Line intensity mapping with [C II] and CO(1-0) as probes of primordial non-Gaussianity,” *Astrophys. J.* **872**, 126 (2019),
- [56] M. B. Silva, M. G. Santos, Y. Gong, A. Cooray, J. Bock, “Intensity Mapping of Lyman-alpha Emission During the Epoch of Reionization”, *Astrophys. J.* **763**, 132 (2013).
- [57] C. Heneka and A. Cooray, “Optimal survey parameters: Ly α and H α intensity mapping for synergy with the 21-cm signal during reionization,” *Mon. Not. Roy. Astron. Soc.* **506**, no.2, 1573-1584 (2021)
- [58] J. L. Bernal, P. C. Breyse and E. D. Kovetz, “Cosmic Expansion History from Line-Intensity Mapping,” *Phys. Rev. Lett.* **123**, 251301 (2019)
- [59] J. L. Bernal, P. C. Breyse, H. Gil-Marín and E. D. Kovetz, “User’s guide to extracting cosmological information from line-intensity maps,” *Phys. Rev. D* **100**, 123522 (2019)
- [60] K. Finish, H. Lazare, S. Libanore, E. Vanzan, J. B. Muñoz, E. D. Kovetz, in prep. (2026).
- [61] H. Lazare, S. Libanore, E. Vanzan, E. D. Kovetz and J. B. Muñoz, in prep. (2026).
- [62] A. T. Crites *et al.*, “The TIME-Pilot intensity mapping experiment”, *Proc. SPIE* **9153**, 91531W (2014).
- [63] E. Visbal and A. Loeb, “Measuring the 3D clustering of undetected galaxies through cross correlation of their cumulative flux fluctuations from multiple spectral lines”, *JCAP* **11**, 016 (2010).